EarthScape: A Multimodal Dataset for Surficial Geologic Mapping and Earth Surface Analysis

Matthew Massey University of Kentucky Lexington, KY 40506, USA

matthew.massey@uky.edu

Abdullah-Al-Zubaer Imran University of Kentucky Lexington, KY 40506, USA

aimran@uky.edu

Abstract

Surficial geologic mapping is essential for understanding Earth surface processes, addressing modern challenges such as climate change and national security, and supporting common applications in engineering and resource management. However, traditional mapping methods are laborintensive, limiting spatial coverage and introducing potential biases. To address these limitations, we introduce Earth-Scape, a novel, AI-ready multimodal dataset specifically designed for surficial geologic mapping and Earth surface analysis. EarthScape integrates high-resolution aerial RGB and near-infrared (NIR) imagery, digital elevation models (DEM), multi-scale DEM-derived terrain features, and hydrologic and infrastructure vector data. The dataset provides detailed annotations for seven distinct surficial geologic classes encompassing various geological processes. We present a comprehensive data processing pipeline using open-sourced raw data and establish baseline benchmarks using different spatial modalities to demonstrate the utility of EarthScape. As a living dataset with a vision for expansion, EarthScape bridges the gap between computer vision and Earth sciences, offering a valuable resource for advancing research in multimodal learning, geospatial analysis, and geological mapping. Our code is available at https://github.com/masseygeo/earthscape.

1. Introduction

Surficial geologic maps are essential tools for addressing contemporary challenges, such as climate change [2], economic and national security interests in critical mineral resources [6, 41], and natural disaster response and mitigation [1, 48]. They depict the spatial distribution of unconsolidated materials on the Earth's surface (Fig. 1), informing applications in urban planning [12], engineering [24], and environmental management [21]. Despite the demonstrable societal benefit and scientific merit, the aerial coverage of surficial geologic

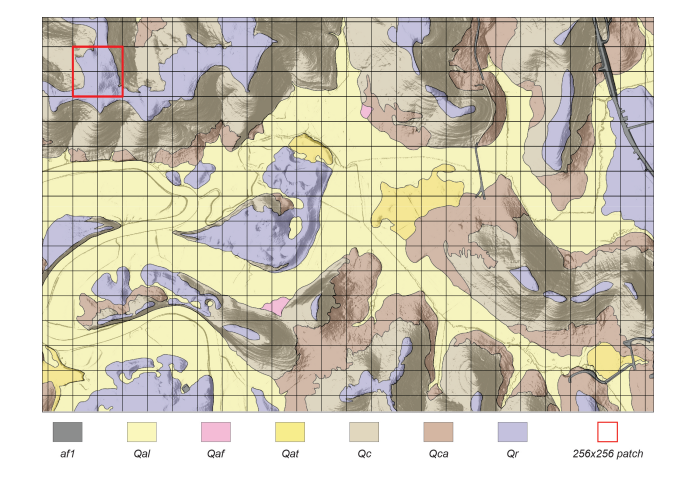


Figure 1. Surficial geologic map showing the seven target classes. The mask is displayed with transparency over hillshade to provide a visual reference between geology and landscape. The grid represents selected EarthScape patches, each measuring 1280 feet (256 pixels) with 50% overlap; red square in upper left shows an example of one patch.

maps is limited due to the time and cost requirements of the manual fieldwork and expert interpretation needed for their production.

Advancements in deep learning and the proliferation of remote sensing imagery present an opportunity to expand surficial geologic mapping, overcoming the limitations of tedious and biased traditional workflows. Recent studies have showcased the power of this type of approach using deep learning models to identify landslides [32, 38, 49] and sinkholes [39]. Several studies have extended these ideas to produce maps of multiple classes of geologic [26, 33, 49] or soil [4] materials. These studies have demonstrated the utility of computer vision (CV) for geological investigations, but this area of research is still in its infancy.

The challenges presented by surficial geological mapping align closely with current trends in CV research. Multimodal fusion of diverse geological datasets is necessary to accurately capture geologic map features (e.g., [3, 28, 43]). The spatial dependencies of geological features resonate with advancements in attention mechanisms (e.g., [15, 19, 37]), multi-scale architectures (e.g., [8, 16, 31]), and contrastive learning methods (e.g., [9, 27, 42]). Geological processes themselves are inherently localized, resulting in spatial distributions of lithologies that are neither evenly nor globally distributed, requiring robust learning techniques to address large class imbalances and improve generalizability (e.g., [18, 29]).

Central to advancing these research directions is the availability of comprehensive, AI-ready datasets specific to geology. CV datasets like ImageNet [14], COCO [30], and CheXpert [22] have been instrumental for progress in object recognition, segmentation, and scene understanding by providing both training data and benchmarks for comparison. There are several datasets specific to remote sensing and land cover classification [11, 13, 44, 47], and one single-class geologic dataset [23], but these lack the specificity for a more generalized geologic dataset. A significant gap exists in the realm of large-scale, multimodal datasets for geological applications, hindering advancements in this domain.

EarthScape is a multimodal dataset focused on surficial geologic mapping, but with a broad applicability to Earth surface analysis. The dataset combines aerial RGB and nearinfrared (NIR) imagery, digital elevation models (DEM), geomorphometric terrain features, and transportation and hydrological networks derived from vector GIS datasets, which are all open source. This multimodal approach captures the complexity of geological environments, providing a rich testbed for advanced CV techniques. This dataset not only provides a robust benchmark, but also presents unique challenges that can drive innovation in CV research, particularly in areas of multimodal learning and geospatial data analysis. As a living dataset with potential for growth, Earth-Scape aims to bridge the gap between CV and Earth sciences, paving the way for more advanced, generalized models in geospatial remote sensing applications. Our primary contributions are as follows:

- We introduce EarthScape, the first AI-ready, multimodal dataset specifically designed to enable the use of advanced CV techniques in surficial geologic mapping and Earth surface analysis.
- We leverage multiscale terrain features to capture geological processes across a range of spatial scales, enhancing model performance.
- We establish benchmarks for multilabel classification, providing a foundation for future research in multimodal data fusion.

2. Related work

Remote sensing: Remote sensing has emerged as a pivotal domain in CV, enabling the analysis and interpretation of

Earth's surface through satellite and aerial imagery. Its applications include land cover classification, urban planning, environmental monitoring, and disaster management, demonstrating its significant impact on both scientific research and practical problem-solving. Well-established remote sensing datasets such as SpaceNet [47], xView [25], and Functional Map of the World [10] provide high-resolution overhead imagery annotated for tasks like classification, object detection, and segmentation. These datasets focus primarily on urban environments and man-made structures, facilitating applications in urban planning, infrastructure monitoring, and disaster response. BigEarthNet [44], DeepGlobe [13], and SEN12MS [40] extend this to land cover classification, but do not address Earth surface processes, and are not designed for geological analysis.

Multimodal learning: Multimodal learning has gained prominence in CV, particularly in remote sensing, where integrating data from different sources enhances the understanding of complex environments. Remote sensing datasets often include various spectral bands, lidar data, and radar imagery, providing complementary information that improves model performance and robustness.. For example, SpaceNet [47], BEN [44], and SEN12MS [40] provide geographically paired multimodal data, including optical imagery and synthetic aperture radar data. These datasets support tasks like land cover classification, change detection, and environmental monitoring, but, again, they are tailored for applications related to land cover and urban environments, lacking the specificity needed for Earth's natural surface processes and geological features.

In geological applications, multimodal AI studies commonly rely on mid-level fusion of DEMs and overhead RGB imagery. This approach can be effective for site-specific tasks where geological features are well-represented by the available sensors [23, 32, 33]. For example, Liu et al. [32] and Zhou et al. [50] achieved success in landslide identification with recent landslides that were well exposed to the satellite sensors, but performance diminished with older landslides obscured by vegetation or altered by erosion.

Several studies have incorporated additional modalities derived from DEMs to enhance geological feature detection. Zhou et al. [50] included elevation contour lines to provide more detailed topographic information. Latifovic et al. [26] and Wang et al. [49] integrated geologic sample analyses, enriching their datasets with ground-truthed geological properties. Liu et al. [33] incorporated aeromagnetic imagery to capture subsurface geological structures.

EarthScape addresses these gaps by offering a comprehensive, AI-ready multimodal dataset specifically designed for geological mapping and Earth surface analysis. It includes paired geologic masks, multiclass labels, RGB and NIR aerial imagery, DEMs, vector infrastructure and hy-

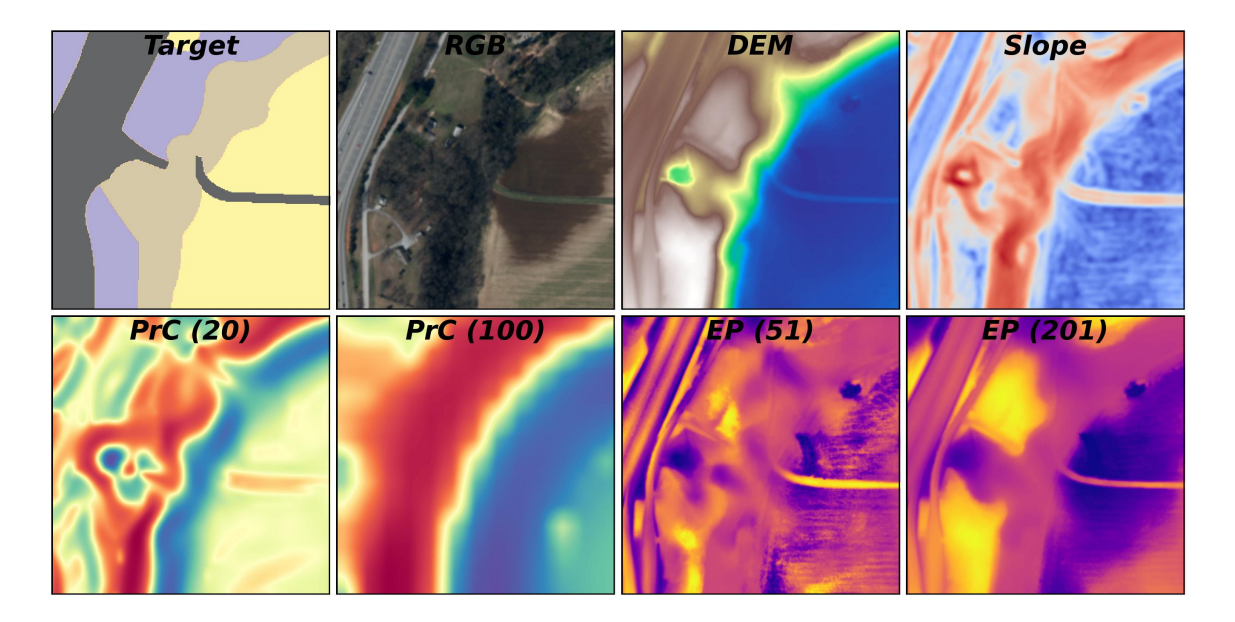


Figure 2. Target mask and selected modalities for one randomly selected EarthScape patch. (top) From left to right: target mask (same colors as Fig. 1, RGB aerial imagery, DEM, and slope. (bottom) From left to right: Profile curvatures from the 20-foot and 100-foot DEMs, and elevation percentile calculated with 51×51 and 201×201 windows.

drological data, and multiple terrain features calculated at various scales. By providing standardized annotations and formats conducive to deep learning, EarthScape facilitates reproducibility and accelerates research at the intersection of computer vision and geosciences.

3. EarthScape Dataset

The EarthScape dataset introduced in this work is a novel, AI-ready, multimodal resource tailored to address surficial geologic mapping challenges via machine learning. This dataset is the first to fuse geospatial geological data with multimodal remote sensing imagery, enabling researchers to complete complex tasks such as multilabel classification and segmentation of Earth surface materials. The Earth-Scape dataset includes labeled surficial geologic maps as segmentation masks and a comprehensive suite of predictive features derived from four publicly accessible geospatial datasets. These multimodal inputs are preprocessed and curated specifically for surficial geological mapping and Earth surface analysis tasks.

3.1. Dataset Composition and Features

Surficial geologic maps: The Kentucky Geological Survey has conducted detailed surficial geologic mapping efforts since 2004, with a focus on supporting growing population centers and transportation corridors across Kentucky. This mapping, most recently completed for Warren and Hardin Counties, is conducted at a scale of 1:24,000 or finer, which

is considered the standard for detailed geological mapping. The geologic maps are available as standardized vector polygons stored in an ESRI file geodatabase. The EarthScape dataset currently includes data from eight maps covering these two regions [5, 7, 20, 34–36, 45, 46].

Seven distinct surficial geologic map units are currently represented in the dataset, capturing three dominant geological processes (Fig. 1, Fig. 2): fluvial transport and deposition, gravitational sedimentation, and in-situ weathering of bedrock. Alluvium (Qal) consists of unconsolidated sediments deposited by active river processes in floodplains and riverbeds. Terrace deposits (Qat) are older deposits of alluvium, but elevated above current floodplains, left behind as rivers incised their valleys. Alluvial fans (Qaf) are fan-shaped deposits formed where high-gradient streams suddenly lose velocity, causing rapid sediment deposition; these deposits can sometimes signify areas prone to hazardous debris flows. Colluvium (Qc) represents unconsolidated materials on slopes that are actively eroding due to gravity, while colluvial aprons (Qca) are more stable deposits found at the bases of slopes. Residuum consists of in-situ weathered material overlying its bedrock parent. Finally, artificial fill (af1) represents anthropogenic materials used to modify landscapes for construction and infrastructure projects. These surficial geologic map units serve as the target labels and segmentation masks within the EarthScape dataset.

Aerial imagery and DEM: The KyFromAbove program has been acquiring high-resolution aerial imagery and DEM

for Kentucky since 2010. The aerial imagery consists of RGB and NIR channels with a 6-inch spatial resolution. Its utility is in identifying anthropogenic features (such as af1) that are easily distinguished from natural landscapes. The NIR band further enhances the detection of hydrological features, such as alluvial deposits and stream channels, by highlighting vegetation patterns that can indicate water presence or recent sediment deposition. While aerial imagery is valuable for recognizing specific landscape elements (Fig. 2), its utility in delineating broader surficial map units is more limited. In contrast, the DEM (Fig. 2), generated from airborne lidar with a 5-foot spatial resolution, is the most critical feature in EarthScape for surficial geologic mapping and Earth surface analysis. Both the DEM and the aerial imagery are available as publicly accessible GeoTIFF tiles. It is important to note that the DEM and aerial imagery were acquired at different times, so temporal discrepancies are present.

Multi-scale terrain features: The DEM serves as the foundation for deriving a suite of geomorphometric terrain features essential for interpreting Earth's surface processes and delineating surficial geologic units. Five key terrain features were calculated at multiple spatial scales to capture both localized and regional topographic variations, which are critical for understanding geological phenomena such as sediment transport, erosion, and landform development (Fig. 2). Slope quantifies the steepness of the terrain, providing insight into processes like erosion and material movement (Fig. 2). Profile curvature helps identify areas where gravitydriven or water flow accelerates or decelerates, influencing patterns of erosion and sediment deposition (Fig. 2). Planform curvature helps detect convergent or divergent flow patterns across the landscape. Standard deviation of slope captures local variability in slope, highlighting areas with complex topography that may correlate with diverse geologic materials or processes. Elevation percentile provides a relative measure of topographic position, distinguishing between features like ridges, valleys, or basins (Fig. 2).

These terrain features provide supplementary topographic data that enhance the interpretation of geological processes, including weathering, drainage patterns, and vegetation, all of which are critical for identifying and delineating surficial geologic units. By computing these features at multiple scales, the EarthScape dataset offers a richer representation of topographic influence at different spatial levels, significantly enhancing its utility for deep learning applications in geology and Earth surface analysis.

Hydrography: The U.S. Geological Survey's National Hydrography Dataset High Resolution (NHDHR) provides detailed vector data for hydrological features, including stream and river centerlines and waterbody polygons, available in

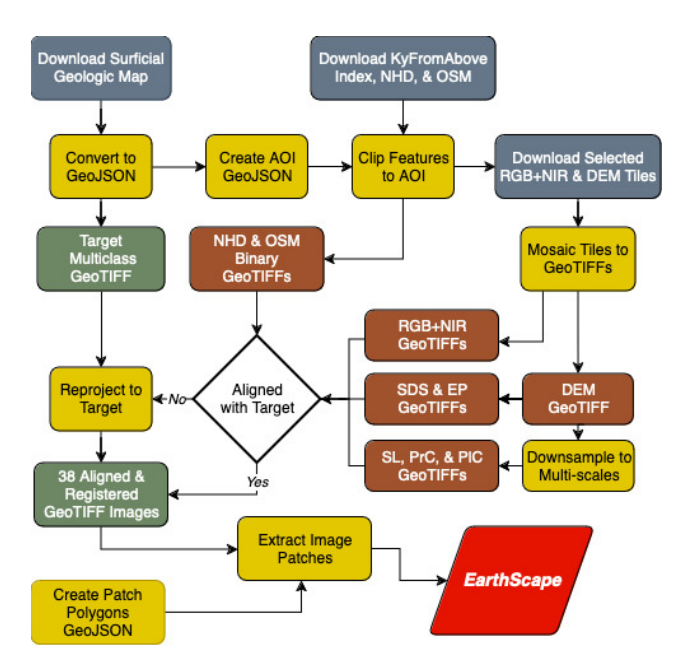


Figure 3. Data processing pipeline for EarthScape.

an ESRI file geodatabase format. These hydrological vectors offer valuable contextual information for surficial geological mapping, as the distribution and dynamics of water bodies often correlate with surface geology. In the EarthScape dataset, these features are particularly useful for identifying and delineating alluvial deposits within stream valleys, where water-driven sediment transport and deposition processes dominate.

Infrastructure: OpenStreetMap (OSM) provides opensource vector data on transportation networks, including road and railway centerlines, available as shapefiles. These infrastructure features were included in the EarthScape dataset to explicitly identify areas where human activity has modified the natural landscape, such as regions with artificial fill. In areas with dense road or railway networks, these features may help the model more quickly learn where surficial geology has been altered by construction or other anthropogenic processes. Additionally, roads and railways can directly influence surficial geology by undercutting slopes, reducing slope stability, and potentially triggering landslides. By integrating OSM data, the EarthScape dataset enables the analysis of these interactions between infrastructure and geological processes.

3.2. Data Processing

Features: Each geologic map was downloaded as a vector GIS geodatabase, the feature class of interest was extracted (Fig. 3), and the vector polygons were inspected for topological correctness, ensuring no overlaps, no gaps, and valid

polygon geometries. The validated data was saved as a standalone GeoJSON file, which was used to generate a boundary polygon defining the area of interest (AOI) for clipping and extracting relevant portions of other datasets (Fig. 3). Each surficial geologic map unit within the GeoJSON was encoded with ordinal values and subsequently rasterized into a GeoTIFF image at a 5-foot spatial resolution, consistent with the DEM.

The KyFromAbove tile index geodatabase contains geospatial polygons representing the locations of aerial RGB+NIR imagery and DEM tiles across Kentucky. Using the target AOI, the relevant tiles covering each map area were isolated, and the corresponding image data were retrieved via URLs embedded in the tile attributes (Fig. 3). The DEM tiles were merged into one seamless GeoTIFF mosaic image with a 5-foot spatial resolution. RGB+NIR imagery tiles were processed using a similar approach but also included steps for separating each of the four spectral channels into a separate mosaic image and downsampling from 6-inch to 5-foot spatial resolution.

Five terrain features were derived directly from the DEM mosaic (Fig. 3). The original DEM, with a 5-foot resolution, was downsampled using cubic convolution to five coarser resolutions of 10, 20, 50, 100, and 200 feet per pixel. A Gaussian filter was applied to each downsampled DEM to smooth potential artifacts and improve terrain feature calculations. Slope, profile curvature, and planform curvature were then computed at each of the six DEM resolutions using 5×5 pixel windows, which capture terrain characteristics from local to global scales. Terrain features were then upsampled back to the original 5-foot resolution using cubic convolution, and another Gaussian filter was applied to minimize resampling artifacts. The standard deviation of slope and elevation percentile were calculated using variable kernel sizes of 5×5 , 11×11 , 21×21 , 51×51 , 101×101 , and 201×201 pixels, applied directly to the original 5-foot DEM. These kernel sizes capture spatial neighborhoods similar to those represented by the coarser-resolution DEM-derived features but are better suited for these specific terrain metrics due to their sensitivity to window size variations. Both slope and standard deviation of slope exhibit a positive skew and were log-transformed to reduce skewness and improve their suitability for downstream analysis.

The NHDHR and OSM vector datasets were downloaded for the entire state of Kentucky, and the AOI boundary was used to clip and extract the relevant features for the target areas (Fig. 3). NHDHR stream centerlines and waterbody polygons and OSM road and railway centerlines were converted into two separate binary images representing the hydrological and infrastructure features.

Spatial alignment and registration: The target geology GeoTIFF image served as the spatial reference for aligning

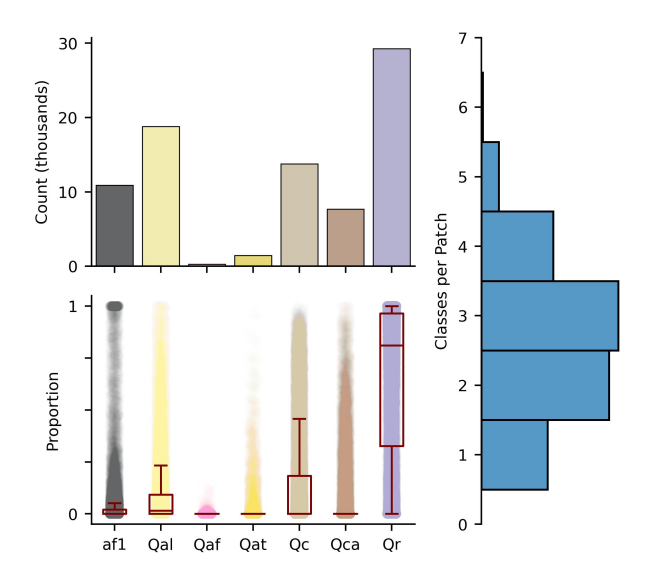


Figure 4. Dataset statistics of total class counts (upper left), distributions of class proportions per patch (bottom left), and number of classes per patch (right). Colors correspond to Figure 1.

all other features in the dataset (Fig. 3). Once each feature was collected and compiled into its respective GeoTIFF image, they were each reprojected and aligned to the reference image coordinates using cubic convolution interpolation. All images were checked to ensure that their bounding coordinates and spatial resolution were consistent across all other images.

Image patches: Vector polygon patches covering the target AOIs were systematically constructed in a grid pattern, each was assigned a unique patch ID, and were saved as GeoJSON files to retain geospatial locations (Fig. 3). Each patch measures 256×256 pixels, overlaps adjacent patches by 50%, and is fully contained within the target AOI. The patch GeoJSON was spatially joined with the target surficial geologic map GeoJSON to calculate both one-hot encoded labels and the proportional areas occupied by each of the seven map units within each patch. Patch polygons were then used to extract 38 image features (excluding the downsampled DEMs), along with their corresponding one-hot labels and proportions (Fig. 3). Each output is named using a standardized format: patch ID, feature name, and file extension (.tif or .csv).

3.3. Dataset Statistics and Challenges

The EarthScape dataset currently comprises 31,018 image patches, each sized 256×256 pixels with 50% overlap, a common setup in remote sensing segmentation tasks [17]. Although EarthScape is designed for immediate use in AI workflows, the accessible code offers flexibility, enabling

users to recreate the dataset with customized patch sizes, overlaps, and augmentation strategies to suit specific requirements. Each patch is saved in GeoTIFF format, providing access to both the image array and geospatial metadata for GIS visualization and spatially aware modeling. The accompanying GeoJSON file containing vector patch polygons supports straightforward visualization of patch locations and spatial visualizations of performance evaluations.

A key challenge addressed by EarthScape is class imbalance, inherent to geological data due to natural geologic processes that vary across scales. This imbalance is apparent both in the overall class distribution and the exposed areas of classes within individual patches (0-100%), where each contains between one and six surficial geologic classes (see Fig. 4).

Generalizability is a core consideration in CV, and Earth-Scape addresses this challenge through the consideration of the inherent variability in geological processes and data collection methodologies. The dataset comprises images from two distinct geographic areas, with 23,566 patches from one contiguous region and 7,452 from another. This spatial diversity supports evaluation of regional generalizability, with plans to expand coverage as additional data becomes available. Multi-scale terrain features provide a means to capture geological processes at local to regional scales. Existing workflows required to produce surficial geologic maps lead to variation in interpretation due to obscured geologic boundaries in the field or differences between geologists. This introduces controlled variability that promotes the development of robust, generalizable features. Finally, EarthScape includes temporally diverse data, with features collected between 2019 and 2024. While these temporal differences may introduce minor inconsistencies between modalities, they also provide an opportunity to enhance the model's ability to generalize across changing Earth surface conditions.

4. Methods

We focus on multilabel classification in this study to gain fundamental insights into how models learn geologic features from different modality data. This approach enables us to systematically assess the effectiveness of different data modalities in distinguishing between various geological materials, which is a critical precursor to tackling more complex tasks like semantic segmentation. Our primary objective is to assess the effectiveness of selected EarthScape modalities on feature learning for surficial geologic classes. The multilabel classification framework is particularly well-suited to this task, as geological materials often co-occur and overlap within the same geographic regions, necessitating models capable of assigning multiple labels to a single instance.

Table 1. Dataset splits for training, validation, and testing.

Split	Images	Percentage (%)
Training	8,416	68.7
Validation	768	6.3
In-domain Testing	1,536	12.5
Cross-domain Testing	1,536	12.5

4.1. Image Patch Selection

This study focuses on five modalities available in the Earth-Scape dataset. The DEM is considered the most fundamental piece of information for surficial geologic mapping and is used as a baseline. Slope, RGB imagery, NIR imagery, profile curvature, and elevation percentile are also incorporated to assess model performance. Slope, profile curvature, and elevation percentile are further tested using multiple scales, chosen through a qualitative assessment of their correlation with landforms.

For the dataset splits, the Warren County subset was used for training, validation, and testing. To ensure spatial independence, we first randomly selected a test set of 1,536 image patches, and then a validation set of 768 image patches, ensuring no overlap with the test set (Table 1). The remaining 8,416 patches that did not overlap with the validation or test sets were used for training. Additionally, to assess generalizability to a geologically similar but unseen area, a second test set of 1,536 images was randomly selected from the Hardin County dataset. To address class imbalance, we also employed oversampling techniques for classes Qaf and Qat, which are extremely localized and uncommon. Oversampling was performed by reusing the same selected patches of these minority classes, which, while inflating the dataset, is necessary to facilitate effective learning of these classes.

All selected image patches were normalized using the mean and standard deviation calculated from their respective modalities over the entire dataset. Since geological processes and resulting features are not restricted to any specific spatial orientation, random horizontal and vertical flips were applied. Random rotations were also applied but restricted to 90-degree increments to ensure consistency between labels and augmented features. This precaution avoids scenarios where small extents of certain classes along patch boundaries could be eliminated due to rotation and padding, while the class label would still indicate their presence.

4.2. Surficial Geologic Mapping (SGMap-Net)

With the introduction of EarthScape, geologic mapping can be performed from multiple spatial modalities. Model development is, therefore, focused on utilizing multimodal data in an efficient manner. We propose surficial geologic mapping network (SGMap-Net) capable of processing different geologic modality data to map to geologic classes. To formulate the problem, we assume a data distribution p(X,Y) sampled iid from the dataset $\mathcal{D}=\{X,Y\}$ where $X=\{x_1,x_2,x_3,\ldots x_N\}$ is the set of data samples and $Y=\{y_1,y_2,y_3,\ldots y_N\}$ is the set of corresponding class labels. Each sample in X contains n different geologic modalities i.e., $x_i=\{m_1,m_2,m_3,\ldots m_n\}$. Considering multilabel classification, each sample can be classified as one or multiple classes. Therefore, each label y_i can be represented as $y_1=c_1,c_2,\ldots c_K$ where K is the total number of classes.

SGMap-Net comprises three components: a standardization module, a feature extractor, and a classification head. As in our introduced EarthScape dataset, different modalities may vary in the channel dimension. In the standardization module, SGMap-Net first performs a 1×1 convolution to standardize the channel dimension to C. For multimodal inputs, different modalities are stacked along the channel dimension before standardization. We leverage the ImageNetpretrained ResNeXt-50 as the feature extractor. Regardless of the input modality, with the standardized input, the feature extractor is fed input of $H \times W \times C$ size. Finally, the classification head consists of two fully-connected (FC) layers. The extracted features from the ResNeXt-50 feature extractor are passed through the FC layers. First, the extracted 2048-dimensional features are reduced to 512 and then the 512-dimensional vector is passed through the second FC layer to predict the K classes. The final class outputs are obtained after sigmoid operation in each of the class predictions from the model.

To address class imbalance in the dataset, we employ a focal loss [29], which adjusts the weighting of classes and focuses on hard-to-classify examples.

5. Experiments

5.1. Implementation Details

Training: All models were trained for 10 epochs using a batch size of 32 and the Adam optimizer with a learning rate of 0.0001. Training was conducted on machines equipped with NVIDIA RTX 3060 and RTX 3080 GPUs. The model exhibiting the lowest validation loss was selected for fine-tuning and evaluation. **Model configuration:** To establish baseline performance for the EarthScape dataset, we conducted experiments using a simple model architecture designed for multilabel classification of surficial geologic map units. This setup allowed for a consistent evaluation of individual modalities, isolating their contributions to classification performance. Evaluation: Performance was assessed using per-label metrics such as accuracy, precision, recall, F1 score, average precision (AP), and area under the receiver operating characteristic curve (AUROC), as well as global metrics including overall accuracy, macro-averaged scores, mean average precision (mAP), Hamming loss, and subset accuracy.

5.2. Results & Discussion

We evaluated nine single modalities and one multimodal sample: (1) DEM, (2) RGB aerial imagery, (3) RGB + NIR, (4) slope, (5) multi-scale slope (Slope MS), (6) profile curvature (PrC), (7) multi-scale profile curvature (PrC MS), (8) elevation percentile (EP), (9) multi-scale elevation percentile (EP MS), (10) DEM and EP. Results showed a notable decline in performance when moving from in-domain to cross-domain areas, particularly with F1, underscoring the challenge of generalization in geospatial tasks.

As reported for the unimodal tests in Tables 2 and 3, the DEM consistently achieved the highest F1-scores, with an in-domain score of 0.635 and a cross-domain score of 0.547. This suggests that topographic data encoded in the DEM is a strong predictor of surficial geologic units, likely because it directly reflects landform variations tied to underlying geology.

EP and EP MS performed nearly as well as the DEM, achieving an in-domain F1 of 0.591 and a cross-domain F1 of 0.492. This highlights the utility of this feature in capturing relative elevation changes, which are critical for distinguishing certain geologic units.

Modalities calculated at multiple scales, such as slope and elevation percentile, generally outperformed their singlescale counterparts. This suggests that incorporating features at varying spatial resolutions captures both localized and regional landform characteristics, improving classification accuracy.

Across all modalities, performance declined in the cross-domain test area, with the best overall F1 dropping from 0.635 (in-domain) to 0.547 (cross-domain) as reported in Table 3. This emphasizes the challenge of applying models trained in one region to geologically distinct areas. Future work could address this through data augmentation, pretraining on diverse regions, or domain adaptation techniques.

Our multimodal experiment using early fusion of the DEM and EP modalities shows strong in-domain performance, however, our unimodal tests significantly outperformed the multimodal approach in a cross-domain setting, suggesting potential overfitting to the training region. This discrepancy may stem from early fusion via channel stacking, which could lead to the model learning domain-specific correlations that fail to generalize. Additionally, redundancy between DEM and elevation percentile may have contributed to feature dominance issues, while differences in statistical distributions across domains could have exacerbated the model's reliance on localized patterns.

The results of these baseline experiments demonstrate the utility of individual modalities for multilabel classification tasks in surficial geologic mapping. The strong performance

Table 2. In-domain evaluation of the proposed SGMap-Net model in mapping from the same dataset. Per class and overall Accuracy and F1 scores have been reported. The best and second-best results are **bolded** and <u>underlined</u>, respectively.

M- 1-1	Accuracy									F1								
Model	af1	Qal	Qaf	Qat	Qc	Qca	Qr	avg		af1	Qal	Qaf	Qat	Qc	Qca	Qr	avg	
DEM	0.787	0.729	0.992	0.887	0.886	0.866	0.934	0.869		0.704	0.788	0.000	0.331	0.887	0.770	0.965	0.635	
RGB	0.702	0.655	0.982	0.959	0.769	0.719	0.932	0.817		0.656	0.766	0.000	0.031	0.771	0.005	0.964	0.456	
RGB+NIR	0.699	0.387	0.986	0.927	0.781	0.777	0.930	0.784		0.601	0.019	0.000	0.282	0.790	0.654	0.964	0.473	
Slope	0.628	0.618	0.788	0.944	0.494	0.710	0.928	0.730		0.003	0.764	0.018	0.023	0.657	0.004	0.963	0.348	
Slope MS	0.628	0.618	0.967	0.932	0.531	0.713	0.932	0.760		0.000	0.764	0.000	0.019	0.658	0.031	0.965	0.348	
PrC	0.628	0.617	0.967	0.942	0.487	0.714	0.932	0.755		0.000	0.763	0.000	0.082	0.655	0.035	0.965	0.357	
PrC MS	0.372	0.617	0.938	0.945	0.488	0.281	0.932	0.653		0.542	0.763	0.000	0.105	0.656	0.439	0.965	0.496	
EP	0.757	0.693	0.991	0.960	0.805	0.808	0.928	0.849		0.650	0.773	0.222	0.000	0.818	0.712	0.962	0.591	
EP MS	0.744	0.686	0.990	0.960	0.794	0.826	0.924	0.846		0.677	0.781	0.000	0.032	0.796	0.711	0.960	0.565	
DEM+EP	0.790	0.740	0.976	0.960	0.873	0.836	0.938	0.873		0.716	0.803	0.051	0.032	0.877	0.745	0.967	0.599	

Table 3. Cross-domain evaluation of the proposed SGMap-Net model in mapping from an out-of-domain dataset. Per class and overall Accuracy and F1 scores have been reported. The best and second-best results are **bolded** and <u>underlined</u>, respectively.

M- 1-1				Accı	ıracy							F	1			
Model	af1	Qal	Qaf	Qat	Qc	Qca	Qr	avg	af1	Qal	Qaf	Qat	Qc	Qca	Qr	avg
DEM	0.760	0.617	0.995	0.910	0.865	0.891	0.984	0.860	0.569	0.686	0.000	0.092	0.808	0.679	0.992	0.547
RGB	0.706	0.560	0.995	0.772	0.719	0.838	0.983	0.796	0.539	0.698	0.000	0.089	0.659	0.000	0.991	0.425
RGB+NIR	0.726	0.454	0.985	0.882	0.687	0.803	0.973	0.787	0.513	0.016	0.000	0.090	0.639	0.499	0.986	0.392
Slope	0.717	0.550	0.765	0.941	0.305	0.827	0.982	0.727	0.000	0.710	0.006	0.165	0.460	0.007	0.991	0.334
Slope MS	0.717	0.550	0.972	0.939	0.400	0.833	0.982	0.770	0.000	0.710	0.000	0.000	0.485	0.045	0.991	0.319
PrC	0.717	0.550	0.975	0.938	0.297	0.834	0.984	0.756	0.000	0.710	0.000	0.020	0.458	0.008	0.992	0.313
PrC MS	0.283	0.551	0.930	0.922	0.297	0.162	0.982	0.590	0.441	0.710	0.000	0.016	0.458	0.279	0.991	0.414
EP	0.804	0.583	0.996	0.951	0.689	0.826	0.982	0.833	0.573	0.684	0.000	0.050	0.467	0.522	0.991	0.470
EP MS	0.749	0.565	0.994	0.949	0.672	0.829	0.971	0.819	0.617	0.709	0.000	0.025	0.580	0.526	0.985	0.492
DEM+EP	0.710	0.544	0.996	0.950	0.520	0.818	0.984	0.789	0.502	0.670	0.000	0.000	0.496	0.561	0.992	0.460

of the DEM and elevation percentile underscores the importance of topographic information in delineating geologic units. However, the decline in cross-domain performance highlights the inherent complexity and regional variability of geologic data.

These findings provide a strong foundation for further exploration of multimodal approaches, where complementary information from modalities like RGB imagery, DEM, and derived terrain features can be fused to enhance performance. Our preliminary experiments indicate challenges with early fusion, and may be better approached with mid-level or late fusion methods and more sophisticated architectures, including attention-based mechanisms, to better capture interactions between modalities, domain adaptation techniques, and/or improved normalization to improve cross-domain generalization. Finally, the inclusion of global datasets for training could further support the development of models capable of handling diverse geological contexts.

6. Conclusions

In this work, we present EarthScape, a new AI-ready multimodal dataset designed specifically for surficial geologic mapping and Earth surface analysis. Combining highresolution aerial imagery, DEMs, multi-scale terrain features, and GIS vector datasets, EarthScape introduces a new paradigm for leveraging multimodal data in geospatial deep learning tasks. Our dataset addresses key challenges such as multimodality and class imbalance, while providing a rich benchmark for multilabel classification and segmentation. Through baseline experiments, we demonstrate the utility of individual modalities and highlight their potential for generalizable geologic mapping across diverse geographic regions. EarthScape's "living" nature ensures its adaptability and relevance as new data and regions are incorporated, making it a valuable resource for both the computer vision and Earth science communities.

While the focus of this paper has been on introducing EarthScape and establishing baseline results using single modalities, our ongoing and future work aims to fully realize the dataset's potential. Current efforts involve developing and evaluating multimodal fusion models, including attention-based and contrastive learning architectures. We are also exploring the application of segmentation models to produce detailed geologic maps at a patch level, further validating the dataset's utility for high-resolution geospatial analysis. Future work will include benchmarking more sophisticated models, improving generalization across regions by testing with additional geographic areas worldwide, and scaling EarthScape to include larger and more diverse

datasets. These efforts aim to provide pretrained models tailored for fine-tuning on region-specific geological tasks, fostering cross-disciplinary collaboration and advancing the state-of-the-art in geospatial AI.

7. Acknowledgements

This work is partially supported by a grant funded by the National Science Foundation (NSF) under Grant number 2344533.

References

- [1] Irasema Alcántara-Ayala. Geomorphology, natural hazards, vulnerability and prevention of natural disasters in developing countries. *Geomorphology*, 47(2-4):107–124, 2002. 1
- [2] Mark G Anderson and Charles E Ferree. Conserving the stage: climate change and the geophysical underpinnings of species diversity. *PloS one*, 5(7):e11554, 2010.
- [3] Tadas Baltrušaitis, Chaitanya Ahuja, and Louis-Philippe Morency. Multimodal machine learning: A survey and taxonomy. *IEEE transactions on pattern analysis and machine* intelligence, 41(2):423–443, 2018.
- [4] Thorsten Behrens, Karsten Schmidt, Robert A MacMillan, and Raphael A Viscarra Rossel. Multi-scale digital soil mapping with deep learning. *Scientific reports*, 8(1):15244, 2018.
- [5] Antonia Bottoms, Max Hammond, Matthew Massey, Emily Morris, and Michelle McHugh. Surficial geologic map of the howe valley 7.5-minute quadrangle, central kentucky. *Kentucky Geological Survey Contract Report*, 13(43), 2021. 3, 11
- [6] George H Brimhall, John H Dilles, and John M Proffett. The role of geologic mapping in mineral exploration. 2005.
- [7] Wes Buchanan, Meredith Swallom, Antonia Bottoms, Matthew Massey, Bailee Nicole Hodelka, and Emily Morris. Surficial geologic map of the rockfield 7.5-minute quadrangle, warren, logan, and simpson counties, kentucky. Kentucky Geological Survey Contract Report, 13(57), 2023. 3, 11
- [8] Liang-Chieh Chen, George Papandreou, Iasonas Kokkinos, Kevin Murphy, and Alan L Yuille. Deeplab: Semantic image segmentation with deep convolutional nets, atrous convolution, and fully connected crfs. *IEEE transactions on pattern* analysis and machine intelligence, 40(4):834–848, 2017. 2
- [9] Ting Chen, Simon Kornblith, Mohammad Norouzi, and Geoffrey Hinton. A simple framework for contrastive learning of visual representations. In *International conference on machine learning*, pages 1597–1607. PMLR, 2020. 2
- [10] Gordon Christie, Neil Fendley, James Wilson, and Ryan Mukherjee. Functional map of the world. In *Proceedings* of the IEEE Conference on Computer Vision and Pattern Recognition, pages 6172–6180, 2018. 2
- [11] Marius Cordts, Mohamed Omran, Sebastian Ramos, Timo Rehfeld, Markus Enzweiler, Rodrigo Benenson, Uwe Franke, Stefan Roth, and Bernt Schiele. The cityscapes dataset for semantic urban scene understanding. In *Proceedings of the IEEE conference on computer vision and pattern recognition*, pages 3213–3223, 2016. 2

- [12] FC Dai, CF Lee, and XH Zhang. Gis-based geoenvironmental evaluation for urban land-use planning: a case study. *Engineering geology*, 61(4):257–271, 2001. 1
- [13] Ilke Demir, Krzysztof Koperski, David Lindenbaum, Guan Pang, Jing Huang, Saikat Basu, Forest Hughes, Devis Tuia, and Ramesh Raskar. Deepglobe 2018: A challenge to parse the earth through satellite images. In *Proceedings of the IEEE conference on computer vision and pattern recognition* workshops, pages 172–181, 2018. 2
- [14] Jia Deng, Wei Dong, Richard Socher, Li-Jia Li, Kai Li, and Li Fei-Fei. Imagenet: A large-scale hierarchical image database. In 2009 IEEE conference on computer vision and pattern recognition, pages 248–255. Ieee, 2009. 2
- [15] Alexey Dosovitskiy. An image is worth 16x16 words: Transformers for image recognition at scale. arXiv preprint arXiv:2010.11929, 2020. 2
- [16] Haoqi Fan, Bo Xiong, Karttikeya Mangalam, Yanghao Li, Zhicheng Yan, Jitendra Malik, and Christoph Feichtenhofer. Multiscale vision transformers. In *Proceedings of the IEEE/CVF international conference on computer vision*, pages 6824–6835, 2021. 2
- [17] Nariman Firoozy, Puyan Mojabi, Tyler Tiede, Thomas Neusitzer, and David G Barber. Normalized radar cross section analysis of oil-contaminated young sea ice. In 2016 USNC-URSI Radio Science Meeting, pages 99–100. IEEE, 2016. 5
- [18] Kushankur Ghosh, Colin Bellinger, Roberto Corizzo, Paula Branco, Bartosz Krawczyk, and Nathalie Japkowicz. The class imbalance problem in deep learning. *Machine Learning*, 113(7):4845–4901, 2024.
- [19] Mohammed Hassanin, Saeed Anwar, Ibrahim Radwan, Fahad Shahbaz Khan, and Ajmal Mian. Visual attention methods in deep learning: An in-depth survey. *Information Fusion*, 108:102417, 2024. 2
- [20] Bailee Hodelka, Matthew Massey, Meredith Swallom, Steve Martin, Charles Wells, and Emily Morris. Surficial geologic map of the bristow 7.5-minute quadrangle, kentucky. Accepted for publication, 2024. 3, 11
- [21] Kelly J Hokanson, CA Mendoza, and KJ Devito. Interactions between regional climate, surficial geology, and topography: characterizing shallow groundwater systems in subhumid, low-relief landscapes. *Water Resources Research*, 55(1):284– 297, 2019.
- [22] Jeremy Irvin, Pranav Rajpurkar, Michael Ko, Yifan Yu, Silviana Ciurea-Ilcus, Chris Chute, Henrik Marklund, Behzad Haghgoo, Robyn Ball, Katie Shpanskaya, et al. Chexpert: A large chest radiograph dataset with uncertainty labels and expert comparison. In *Proceedings of the AAAI conference on artificial intelligence*, pages 590–597, 2019.
- [23] Shunping Ji, Dawen Yu, Chaoyong Shen, Weile Li, and Qiang Xu. Landslide detection from an open satellite imagery and digital elevation model dataset using attention boosted convolutional neural networks. *Landslides*, 17:1337–1352, 2020.
- [24] Jeffrey R Keaton. Engineering geology: fundamental input or random variable? In Foundation Engineering in the Face of Uncertainty: Honoring Fred H. Kulhawy, pages 232–253. 2013.

- [25] Darius Lam, Richard Kuzma, Kevin McGee, Samuel Dooley, Michael Laielli, Matthew Klaric, Yaroslav Bulatov, and Brendan McCord. xview: Objects in context in overhead imagery. arXiv preprint arXiv:1802.07856, 2018. 2
- [26] Rasim Latifovic, Darren Pouliot, and Janet Campbell. Assessment of convolution neural networks for surficial geology mapping in the south rae geological region, northwest territories, canada. *Remote sensing*, 10(2):307, 2018. 1, 2
- [27] Phuc H Le-Khac, Graham Healy, and Alan F Smeaton. Contrastive representation learning: A framework and review. *Ieee Access*, 8:193907–193934, 2020. 2
- [28] Hui Li and Xiao-Jun Wu. Crossfuse: A novel cross attention mechanism based infrared and visible image fusion approach. *Information Fusion*, 103:102147, 2024. 2
- [29] T Lin. Focal loss for dense object detection. arXiv preprint arXiv:1708.02002, 2017. 2, 7
- [30] Tsung-Yi Lin, Michael Maire, Serge Belongie, James Hays, Pietro Perona, Deva Ramanan, Piotr Dollár, and C Lawrence Zitnick. Microsoft coco: Common objects in context. In Computer Vision–ECCV 2014: 13th European Conference, Zurich, Switzerland, September 6-12, 2014, Proceedings, Part V 13, pages 740–755. Springer, 2014. 2
- [31] Sihan Liu, Yiwei Ma, Xiaoqing Zhang, Haowei Wang, Jiayi Ji, Xiaoshuai Sun, and Rongrong Ji. Rotated multi-scale interaction network for referring remote sensing image segmentation. In Proceedings of the IEEE/CVF Conference on Computer Vision and Pattern Recognition, pages 26658–26668, 2024. 2
- [32] Xinran Liu, Yuexing Peng, Zili Lu, Wei Li, Junchuan Yu, Daqing Ge, and Wei Xiang. Feature-fusion segmentation network for landslide detection using high-resolution remote sensing images and digital elevation model data. *IEEE Transactions on Geoscience and Remote Sensing*, 61:1–14, 2023.
- [33] Yao Liu, Jianyuan Cheng, Qingtian Lü, Zaibin Liu, Jingjin Lu, Zhenyu Fan, and Lianzhi Zhang. Deep learning for geological mapping in the overburden area. *Frontiers in Earth Science*, 12:1407173, 2024. 1, 2
- [34] Matthew Massey, Antonia Bottoms, Max Hammond, Emily Morris, and Michelle McHugh. Surficial geologic map of the sonora 7.5-minute quadrangle, central kentucky. *Kentucky Geological Survey Contract Report*, 13(44), 2021. 3, 11
- [35] Matthew Massey, Meredith Swallom, Antonia Bottoms, Wes Buchanan, Bailee Nicole Hodelka, and Emily Morris. Surficial geologic map of the hadley 7.5-minute quadrangle, warren county, kentucky. *Kentucky Geological Survey Contract Report*, 13(56), 2023. 11
- [36] Matthew Massey, Meredith Swallom, Bailee Hodelka, Hannah Hayes, Charles Wells, Steve Martin, and Emily Morris. Surficial geologic map of the bowling green south 7.5-minute quadrangle, kentucky. Accepted for publication, 2024. 3, 11
- [37] Zhaoyang Niu, Guoqiang Zhong, and Hui Yu. A review on the attention mechanism of deep learning. *Neurocomputing*, 452:48–62, 2021.
- [38] Nikhil Prakash, Andrea Manconi, and Simon Loew. A new strategy to map landslides with a generalized convolutional neural network. *Scientific reports*, 11(1):9722, 2021. 1

- [39] Muhammad Usman Rafique, Junfeng Zhu, and Nathan Jacobs. Automatic segmentation of sinkholes using a convolutional neural network. *Earth and Space Science*, 9(2): e2021EA002195, 2022.
- [40] Michael Schmitt, Lloyd Haydn Hughes, Chunping Qiu, and Xiao Xiang Zhu. Sen12ms–a curated dataset of georeferenced multi-spectral sentinel-1/2 imagery for deep learning and data fusion. arXiv preprint arXiv:1906.07789, 2019. 2
- [41] Klaus J Schulz. Critical mineral resources of the United States: economic and environmental geology and prospects for future supply. Geological Survey, 2017. 1
- [42] B Song, Y Xu, and Y Wu. Vitcn: Vision transformer contrastive network for reasoning. arxiv preprint. arXiv preprint arXiv:2403.09962, 2024.
- [43] Sandra Steyaert, Marija Pizurica, Divya Nagaraj, Priya Khandelwal, Tina Hernandez-Boussard, Andrew J Gentles, and Olivier Gevaert. Multimodal data fusion for cancer biomarker discovery with deep learning. *Nature machine intelligence*, 5 (4):351–362, 2023. 2
- [44] Gencer Sumbul, Marcela Charfuelan, Begüm Demir, and Volker Markl. Bigearthnet: A large-scale benchmark archive for remote sensing image understanding. In IGARSS 2019-2019 IEEE International Geoscience and Remote Sensing Symposium, pages 5901–5904. IEEE, 2019. 2
- [45] Meredith Swallom, Matthew Massey, Wes Buchanan, Bailee Nicole Hodelka, Hannah Hayes, Charles Wells III, and Emily Morris. Surficial geologic map of the bowling green north 7.5-minute quadrangle, warren county, kentucky. *Kentucky Geological Survey Contract Report*, 13(55), 2023. 3, 11
- [46] Meredith Swallom, Bailee Hodelka, Matthew Massey, Hannah Hayes, Charles Wells, and Emily Morris. Surficial geologic map of the smiths grove 7.5-minute quadrangle, kentucky. Accepted for publication, 2024. 3, 11
- [47] Adam Van Etten, Dave Lindenbaum, and Todd M Bacastow. Spacenet: A remote sensing dataset and challenge series. *arXiv preprint arXiv:1807.01232*, 2018. 2
- [48] CJ Van Westen, N Rengers, and R Soeters. Use of geomorphological information in indirect landslide susceptibility assessment. *Natural hazards*, 30:399–419, 2003. 1
- [49] Ziye Wang, Renguang Zuo, and Hao Liu. Lithological mapping based on fully convolutional network and multi-source geological data. *Remote Sensing*, 13(23):4860, 2021. 1, 2
- [50] Yiming Zhou, Yuexing Peng, Wei Li, Junchuan Yu, Daqing Ge, and Wei Xiang. A hyper-pixel-wise contrastive learning augmented segmentation network for old landslide detection using high-resolution remote sensing images and digital elevation model data. *arXiv preprint arXiv:2308.01251*, 2023.

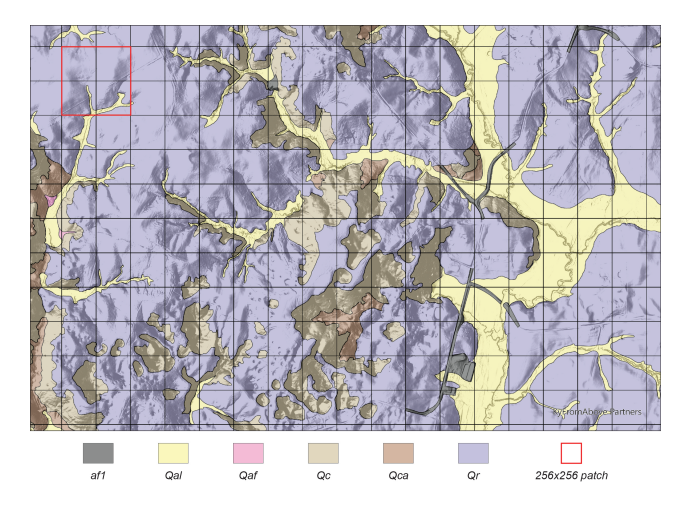


Figure 5. Surficial geologic map of part of Hardin County showing six target classes. As seen in the main paper, this map highlights similar terrain characteristics and surficial geologic units. The geologic mask is overlaid with transparency on a hillshade image to highlight the relationship between geologic features and landscape. The grid represents EarthScape patches, each measuring 1280 feet (256 pixels) with 50% overlap. The red square in the upper left outlines one example patch for scale.

A. Exploring the EarthScape Dataset

EarthScape is a geospatially aligned collection of multimodal data designed for surficial geologic mapping and Earth surface analysis. This section provides visual examples that highlight its potential for advancing CV applications in Earth sciences.

Fig. 5 illustrates a surficial geologic map from the Hardin County area in EarthScape, overlaid with transparency on a hillshade image to highlight the interplay between geology and topography. Distinct landforms, such as river valleys and steep slopes, are clearly delineated by their geological units. This visualization is meant to aid the reader in understanding the geological processes and how EarthScape bridges this domain with CV.

Fig. 6 shows the current geographic extent of the Earth-Scape dataset, including two spatially independent regions. Currently, the Warren County area comprises the most data in EarthScape, while the Hardin County area provides a separate area with similar geologic processes to test generalizability. This visualization underscores the dataset's spatial coverage that provides a robust foundation for training and evaluating models on both local and regional scales. As EarthScape is a "living" dataset, more areas will be added on a rolling basis to increase data diversity, geographic extent, and new surficial geologic target classes.

Figs. 7 and 8 showcase the multimodal and multi-scale data available for each of the 31,018 patches in EarthScape. Each mosaic includes all 38 channels, representing expert

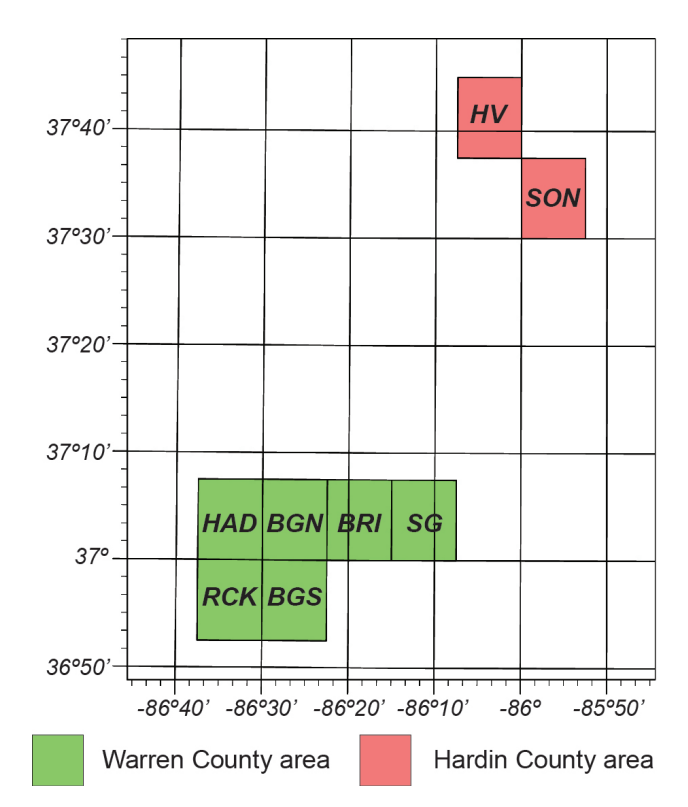


Figure 6. Current geospatial extent of the EarthScape dataset, highlighting coverage in Warren County (green rectangles) and Hardin County (red rectangles). The grid represents latitude and longitude in the NAD83 geographic coordinate reference system. Additional regions will be incorporated into EarthScape on a rolling basis as the dataset evolves. Abbreviations correspond to the original published geologic maps: RCK (Rockfield) [7], HAD (Hadley) [35], BGN (Bowling Green North) [45], BGS (Bowling Green South) [36], BRI (Bristow) [20], SG (Smiths Grove) [46], HV (Howe Valley) [5], and SON (Sonora) [34].

annotated masks for the target classes, aerial imagery, DEM and derived features, and vector data. Collectively, these channels capture diverse and complementary information for surficial geologic mapping and, more broadly, Earth surface analysis. The visualizations emphasize the dataset's potential for advancing multimodal learning in geospatial contexts.

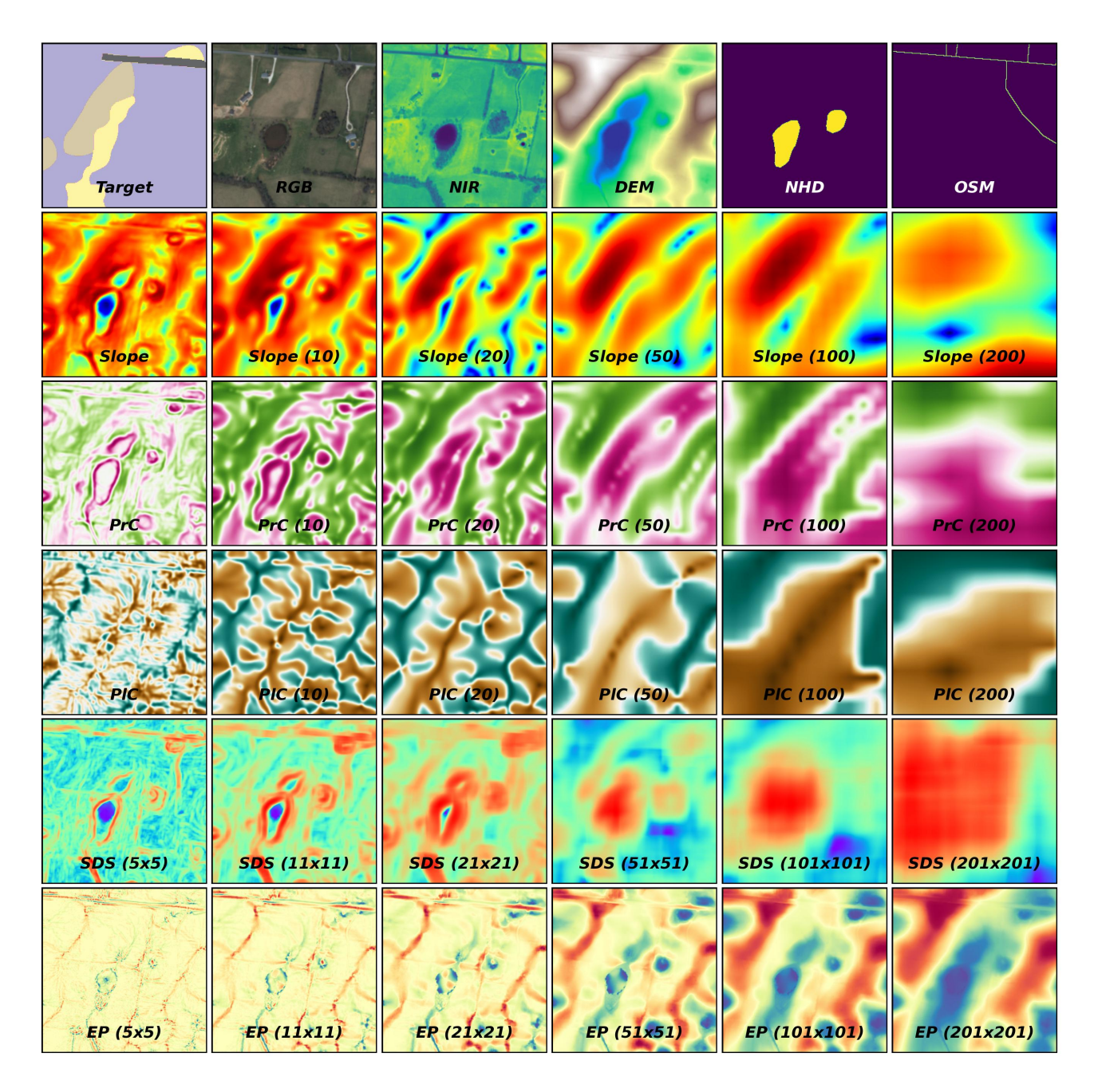


Figure 7. Example patch from the Warren County area showcasing the 38 channels available in EarthScape. Channels are displayed from top left to bottom right: target mask, RGB aerial imagery, NIR aerial imagery, DEM, hydrologic features (NHD), infrastructure (OSM), multiple scales of slope, profile curvature (PrC), planform curvature (PlC) derived from downsampled DEMs, and multiple scales of standard deviation of slope (SDS) and elevation percentile (EP) calculated using multiple window sizes with the original DEM.

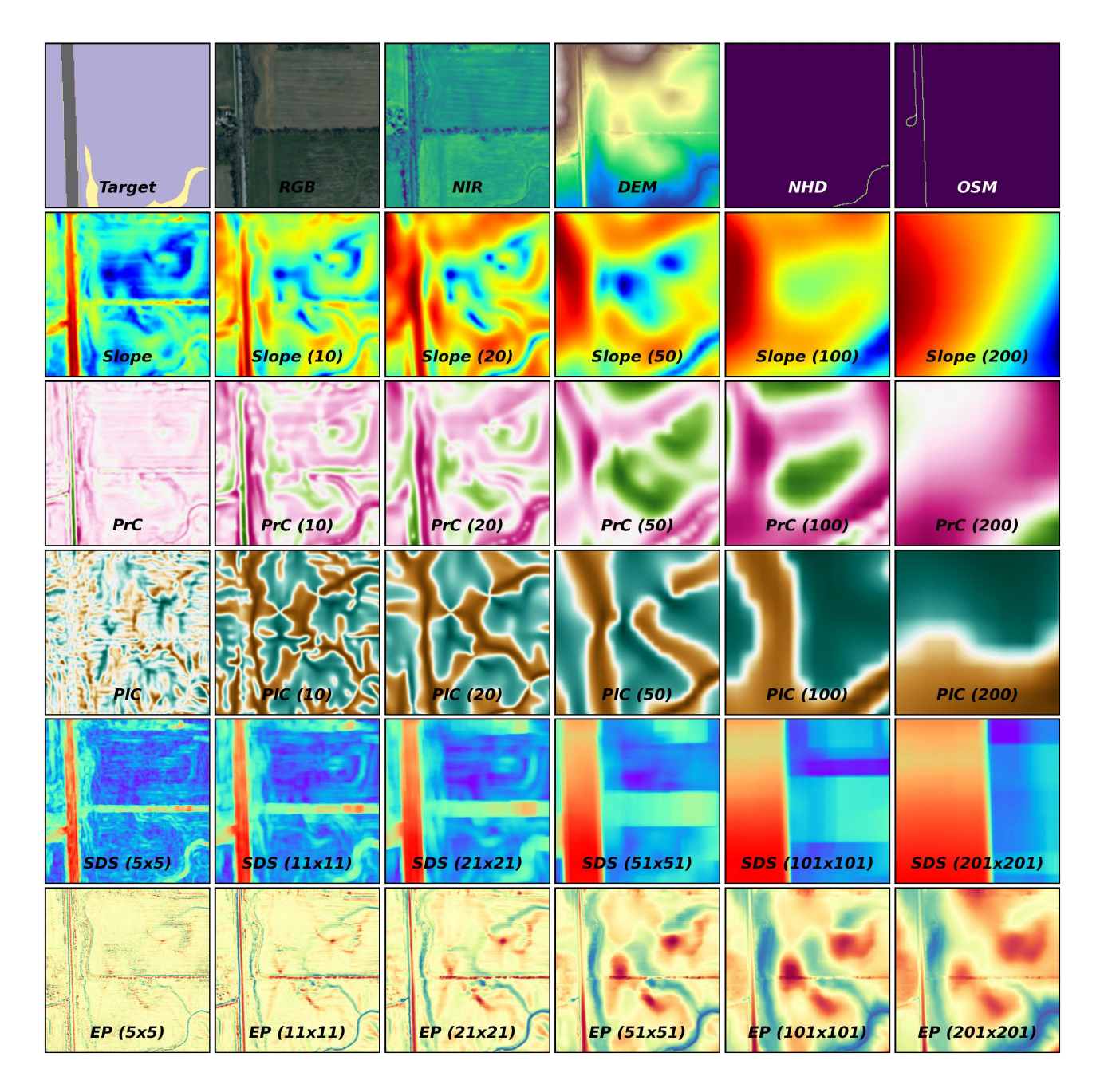


Figure 8. Example patch from the Hardin County area showcasing the 38 channels available in EarthScape. Channels are displayed from top left to bottom right: target mask, RGB aerial imagery, NIR aerial imagery, DEM, hydrologic features (NHD), infrastructure (OSM), multiple scales of slope, profile curvature (PrC), planform curvature (PlC) derived from downsampled DEMs, and multiple scales of standard deviation of slope (SDS) and elevation percentile (EP) calculated using multiple window sizes with the original DEM.

B. Geospatial Patch Selection and Experimental Design

Patch selection for our SGMap-Net model using the Earth-Scape was designed to ensure spatial independence between training, validation, and testing splits, addressing the challenge posed by overlapping patches. The Warren County area was selected for in-domain evaluation due to its more extensive data coverage (Fig. 9). To ensure spatial independence, we first randomly selected 1,536 test patches, followed by 768 validation patches that did not overlap the test set, and then used the remaining 8,416 non-overlapping patches for training. This methodology avoids spatial leakage and enables robust in-domain evaluation. We used an additional randomly selected cross-domain test set of 1,536 patches from the Hardin County area (see Fig. 6) to assess model generalizability in a geographically separate, but geologically similar area. Fig. 10 shows the class distributions across the training, validation, in-domain test, and crossdomain test splits. All splits are highly imbalanced, which reflects natural variation from localized geological processes. Fig. 10 also shows that the distributions of each split are consistent, which ensures that model performance evaluation is not biased by differences in data representation.

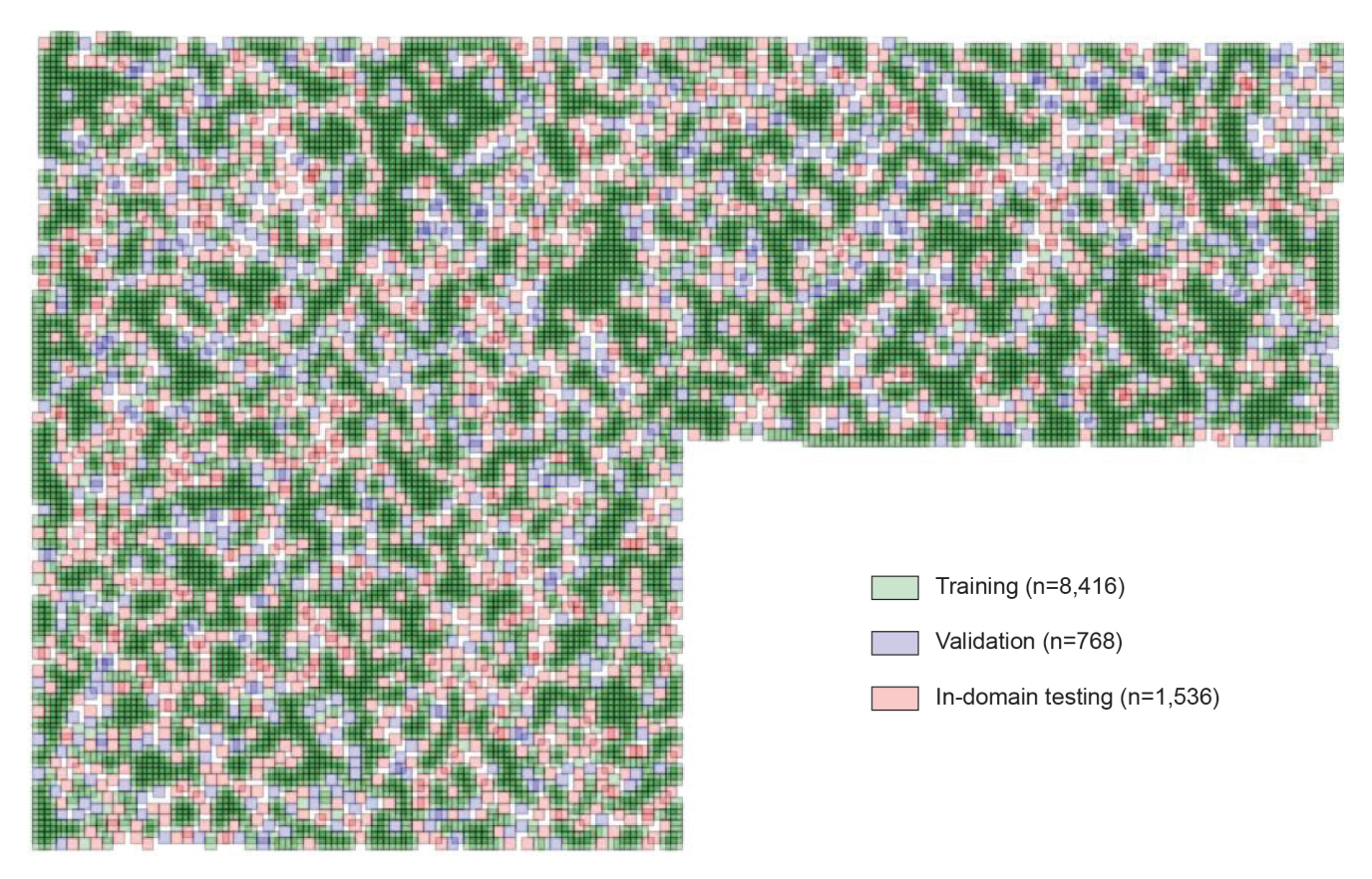


Figure 9. Spatially independent training, validation, and in-domain testing splits from the Warren County area. Note that patches within each split may overlap with other patches in the same split but remain independent across splits.

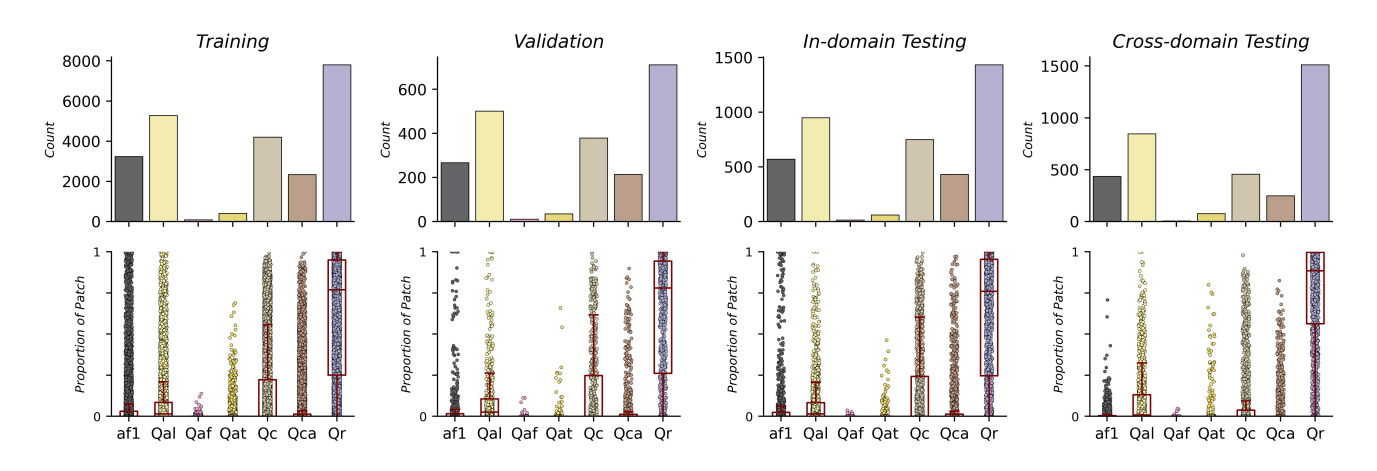


Figure 10. Dataset statistics showing total class counts (left) and class proportions per patch (right) across the training, validation, in-domain testing, and cross-domain testing splits. Colors correspond to those in Figure 1.

C. Performance Analysis and Geographic Insights

The performance of our CV models trained on the Earth-Scape dataset offers valuable insights into the challenges and opportunities of multimodal and multilabel classification for geological mapping. This section presents detailed analyses of model results (Figs 11; Tables 5 and 6), as well as trends across different regions and classes (Fig. 12).

We evaluated SGMap-Net's performance across multiple individual modalities from the EarthScape dataset, including DEM, RGB, RGB+NIR, slope, profile curvature (PrC), PrC at multiple scales (PrC MS), elevation percentile (EP), and EP at multiple scales (EP MS). Training and validation metrics for all SGMap-Net models showed consistent learning between 3 to 9 epochs, after which validation loss began to diverge and overfit (Fig. 11). The best model was selected at the point of lowest validation loss.

Figure 12 compares AUC scores for the two best performing modalities, DEM and EP, across in-domain and cross-domain test splits. While the DEM model often achieved higher absolute AUC scores, the EP model demonstrated much smaller differences between the in-domain and cross-domain splits, indicating better generalization. Table 4 summarizes these differences. This aligns with EP's encoding of relative topographic position rather than absolute elevation of the DEM, making it more robust to domain shifts. These findings suggest that modality selection should consider both in-domain performance and generalization requirements. Table 4 summarizes the ΔAUC scores.

Tables 5 and 6 summarize SGMap-Net's performance on the in-domain and cross-domain test splits, respectively. The DEM and EP models demonstrate the best precision, AP, and AUC scores across most target classes. In contrast, slope and PrC achieved higher recall, likely due to their sensitivity to subtle topographic variations. Cross-domain performance is similar to in-domain performance, but with lower overall scores. These results underscore the importance of modality-specific information in capturing different geological features.

Table 4. Analysis of In-domain vs Cross-domain AUC differences (Δ AUC) for each class across the SGMap-Net DEM and EP models to complement the visualization in figure 12. The best results are **bolded**.

Madal				$\Delta \mathrm{AUC}$			
Model	af1	Qal	Qaf	Qat	Qc	Qca	Qr
DEM	0.055	0.146	0.384	0.375	0.012	0.012	0.22
EP	0.012	0.085	0.056	0.144	0.205	0.046	0.025

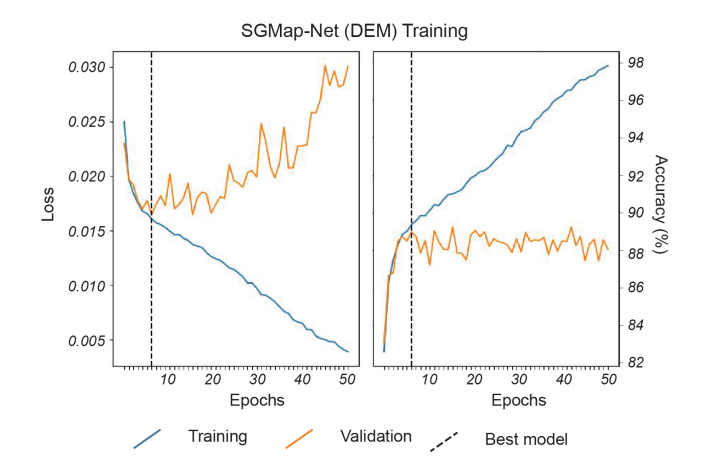


Figure 11. Training and validation loss (left) and accuracy (right) plotted against epochs for the SGMap-Net DEM model. The vertical dashed line indicates the epoch at which the model with the lowest validation loss was retained for fine-tuning and testing.

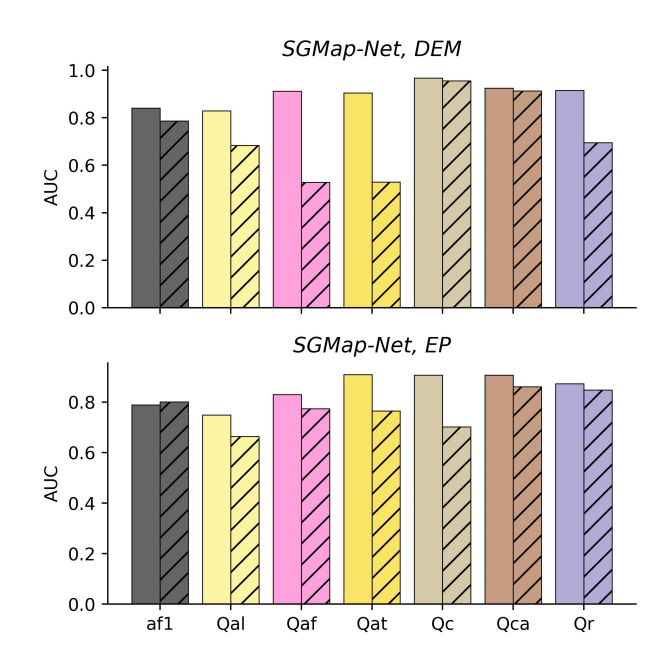


Figure 12. Bar chart comparing in-domain (solid) and cross-domain (hatched) AUC scores for each target class in the SGMap-Net DEM and EP models. Adjacent bars highlight the performance differences between the two test areas. See Table 4 for in-domain-cross-domain difference values.

Table 5. In-domain evaluation of the proposed SGMap-Net model using the Warren County test split. Metrics reported include per-class and overall average precision (AP), recall, area under the receiver operating characteristic curve (AUC), and their macro averages (avg). The best results are **bolded**, and the second-best results are underlined.

				Prec	ision								Re	call			
Model	af1	Qal	Qaf	Qat	Qc	Qca	Qr	avg		af1	Qal	Qaf	Qat	Qc	Qca	Qr	avg
DEM	0.798	0.902	0.170	0.254	0.969	0.858	0.993	0.608		0.841	0.829	0.912	0.904	0.967	0.925	0.915	0.701
RGB	0.575	0.659	0.000	0.250	0.746	0.500	0.937	0.524		0.764	0.916	0.000	0.016	0.798	0.002	0.994	0.499
RGB+NIR	0.592	0.818	0.000	0.232	0.742	0.581	0.941	0.558		0.609	0.009	0.000	0.361	0.844	0.748	0.987	0.508
Slope	0.500	0.618	0.009	0.037	0.491	0.067	0.933	0.379		0.002	1.000	0.231	0.016	0.995	0.002	0.995	0.463
Slope MS	0.000	0.618	0.000	0.022	0.511	0.304	0.933	0.341		0.000	1.000	0.000	0.016	0.927	0.016	0.999	0.423
PrC	0.000	0.618	0.000	0.111	0.487	0.348	0.933	0.357		0.000	0.999	0.000	0.066	0.999	0.019	0.999	0.44
PrC MS	0.372	0.617	0.000	0.147	0.488	0.281	0.933	0.405		1.000	0.997	0.000	0.082	1.000	1.000	0.999	0.725
EP	0.698	0.713	0.400	0.000	0.751	0.616	0.942	0.589		0.608	0.843	0.154	0.000	0.899	0.845	0.983	0.619
EP MS	0.638	0.685	0.000	0.500	0.770	0.665	<u>0.951</u>	0.601		0.720	0.909	0.000	0.016	0.824	0.764	0.969	0.600
DEM+EP	0.722	0.753	0.038	0.500	0.832	0.661	0.949	0.637		0.709	0.860	0.077	0.016	0.927	0.854	0.987	0.633
Model		AP								AUC							
Model	af1	Qal	Qaf	Qat	Qc	Qca	Qr	avg	_	af1	Qal	Qaf	Qat	Qc	Qca	Qr	avg
DEM	0.798	0.902	0.170	0.254	0.969	0.858	0.993	0.707		<u>0.841</u>	0.829	0.912	0.904	0.967	0.925	<u>0.915</u>	0.899
RGB	0.725	0.747	0.017	0.118	0.873	0.622	0.973	0.582		0.792	0.663	0.713	0.752	0.866	0.823	0.769	0.768
RGB+NIR	0.678	0.741	0.03	0.225	0.876	0.616	0.975	0.592		0.753	0.664	0.778	0.794	0.872	0.827	0.784	0.782
Slope	0.395	0.627	0.016	0.043	0.368	0.202	0.919	0.367		0.527	0.512	0.571	0.520	0.294	0.327	0.419	0.453
Slope MS	0.344	0.623	0.013	0.038	0.468	0.462	0.946	0.414		0.449	0.499	0.569	0.469	0.517	0.735	0.610	0.55
PrC	0.364	0.687	0.009	0.062	0.511	0.333	0.937	0.415		0.495	0.557	0.471	0.575	0.462	0.566	0.527	0.522
PrC MS	0.368	0.63	0.007	0.079	0.600	0.301	0.946	0.419		0.508	0.492	0.370	0.650	0.566	0.531	0.576	0.528
EP	0.748	0.837	0.103	0.331	0.910	0.804	0.989	0.675		0.789	0.749	0.830	0.909	0.907	0.907	0.873	0.852
EP MS	0.759	0.849	0.050	0.285	0.875	0.796	0.989	0.658		0.805	0.764	0.801	0.848	0.884	0.893	0.874	0.838
DEM+EP	0.807	0.903	0.071	0.304	0.958	0.841	0.994	0.697		0.846	0.836	0.841	0.902	0.956	0.918	0.920	0.888

Table 6. Cross-domain evaluation of the proposed SGMap-Net model using the Hardin County test split. Metrics reported include per-class and overall average precision (AP), recall, area under the receiver operating characteristic curve (AUC), and their macro averages (avg). The best results are bolded, and the second-best results are $\underline{underlined}$.

Model				Prec	ision								Re	call			
Model	af1	Qal	Qaf	Qat	Qc	Qca	Qr	avg		af1	Qal	Qaf	Qat	Qc	Qca	Qr	avg
DEM	0.578	0.624	0.000	0.092	0.700	0.651	0.984	0.518		0.561	0.762	0.000	0.091	0.954	0.711	1.000	0.583
RGB	0.484	0.561	0.000	0.055	<u>0.515</u>	0.000	0.984	0.371		0.607	0.924	0.000	0.221	0.914	0.000	0.999	0.524
RGB+NIR	0.516	1.000	0.000	0.073	0.486	0.424	0.985	0.498		0.510	0.008	0.000	0.117	0.932	0.606	0.987	0.452
Slope	0.000	0.550	0.003	0.281	0.299	0.056	0.984	0.310		0.000	1.000	0.167	0.117	0.998	0.004	0.997	0.469
Slope MS	0.000	0.550	0.000	0.000	0.325	0.300	0.984	0.308		0.000	1.000	0.000	0.000	0.950	0.024	0.998	0.425
PrC	0.000	0.550	0.000	0.048	0.297	0.125	0.984	0.286		0.000	1.000	0.000	0.013	1.000	0.004	0.999	0.431
PrC MS	0.283	0.551	0.000	0.022	0.297	0.162	0.984	0.328		0.998	0.998	0.000	0.013	1.000	1.000	0.999	0.715
EP	0.748	0.586	0.000	0.667	0.476	0.471	0.984	0.562		0.464	0.822	0.000	0.026	0.458	0.586	0.999	0.479
EP MS	0.544	0.561	0.000	0.333	0.468	0.477	0.984	0.481		0.713	0.963	0.000	0.013	0.763	0.586	0.987	0.575
DEM+EP	0.488	0.557	0.000	0.000	0.360	0.461	0.984	0.407		0.517	0.841	0.000	0.000	0.796	0.715	1.000	0.553
	AP																
Model				A	P								ΑŪ	JC			
Model	af1	Qal	Qaf	A Qat	.P Qc	Qca	Qr	avg		af1	Qal	Qaf	Al Qat	JC Qc	Qca	Qr	avg
Model DEM	af1 0.637	Qal 0.742	Qaf 0.011			Qca 0.694	Qr 0.993	avg 0.579		af1	Qal 0.683	Qaf 0.528			Qca 0.913	Qr 0.695	avg 0.727
				Qat	Qc				-				Qat	Qc			
DEM	0.637	0.742	0.011	Qat 0.074	Qc 0.900	0.694	0.993	0.579	-	0.786	0.683	0.528	Qat 0.529	Qc 0.955	0.913	0.695	0.727
DEM RGB	0.637 0.563	0.742 0.641	0.011 0.004	Qat 0.074 0.058	Qc 0.900 <u>0.778</u>	0.694 0.303	0.993 0.990	0.579 0.477	-	0.786 0.739	0.683 0.591	0.528 0.38	Qat 0.529 0.559	Qc 0.955 <u>0.891</u>	0.913 0.761	0.695 0.619	0.727 0.649
DEM RGB RGB+NIR	0.637 0.563 0.493	0.742 0.641 0.571	0.011 0.004 0.003	Qat 0.074 0.058 0.077	Qc 0.900 <u>0.778</u> 0.761	0.694 0.303 0.384	0.993 0.990 <u>0.994</u>	0.579 0.477 0.469	-	0.786 0.739 0.716	0.683 0.591 0.513	0.528 0.38 0.317	Qat 0.529 0.559 0.514	Qc 0.955 0.891 0.875	0.913 0.761 0.814	0.695 0.619 <u>0.776</u>	0.727 0.649 0.647
DEM RGB RGB+NIR Slope	0.637 0.563 0.493 0.305	0.742 0.641 0.571 0.570	0.011 0.004 0.003 0.006	Qat 0.074 0.058 0.077 0.134	Qc 0.900 0.778 0.761 0.195	0.694 0.303 0.384 0.100	0.993 0.990 <u>0.994</u> 0.974	0.579 0.477 0.469 0.326	-	0.786 0.739 0.716 0.512	0.683 0.591 0.513 0.490	0.528 0.38 0.317 0.508	Qat 0.529 0.559 0.514 0.595	Qc 0.955 0.891 0.875 0.242	0.913 0.761 0.814 0.220	0.695 0.619 <u>0.776</u> 0.316	0.727 0.649 0.647 0.412
DEM RGB RGB+NIR Slope Slope MS	0.637 0.563 0.493 0.305 0.266	0.742 0.641 0.571 0.570 0.580	0.011 0.004 0.003 0.006 0.003	Qat 0.074 0.058 0.077 0.134 0.030	Qc 0.900 0.778 0.761 0.195 0.302	0.694 0.303 0.384 0.100 0.346	0.993 0.990 <u>0.994</u> 0.974 0.986	0.579 0.477 0.469 0.326 0.359	-	0.786 0.739 0.716 0.512 0.466	0.683 0.591 0.513 0.490 0.533	0.528 0.38 0.317 0.508 0.355	Qat 0.529 0.559 0.514 0.595 0.238	Qc 0.955 0.891 0.875 0.242 0.556	0.913 0.761 0.814 0.220 0.792	0.695 0.619 <u>0.776</u> 0.316 0.652	0.727 0.649 0.647 0.412 0.513
DEM RGB RGB+NIR Slope Slope MS PrC	0.637 0.563 0.493 0.305 0.266 0.269	0.742 0.641 0.571 0.570 0.580 0.652	0.011 0.004 0.003 0.006 0.003 0.004	Qat 0.074 0.058 0.077 0.134 0.030 0.072	Qc 0.900 0.778 0.761 0.195 0.302 0.261	0.694 0.303 0.384 0.100 0.346 0.151	0.993 0.990 <u>0.994</u> 0.974 0.986 0.987	0.579 0.477 0.469 0.326 0.359 0.342	-	0.786 0.739 0.716 0.512 0.466 0.484	0.683 0.591 0.513 0.490 0.533 0.611	0.528 0.38 0.317 0.508 0.355 0.415	Qat 0.529 0.559 0.514 0.595 0.238 0.588	Qc 0.955 0.891 0.875 0.242 0.556 0.413	0.913 0.761 0.814 0.220 0.792 0.461	0.695 0.619 0.776 0.316 0.652 0.597	0.727 0.649 0.647 0.412 0.513 0.51
DEM RGB RGB+NIR Slope Slope MS PrC PrC MS	0.637 0.563 0.493 0.305 0.266 0.269 0.290	0.742 0.641 0.571 0.570 0.580 0.652 0.586	0.011 0.004 0.003 0.006 0.003 0.004 0.005	Qat 0.074 0.058 0.077 0.134 0.030 0.072 0.044	Qc 0.900 0.778 0.761 0.195 0.302 0.261 0.422	0.694 0.303 0.384 0.100 0.346 0.151 0.231	0.993 0.990 <u>0.994</u> 0.974 0.986 0.987 0.989	0.579 0.477 0.469 0.326 0.359 0.342 0.367	-	0.786 0.739 0.716 0.512 0.466 0.484 0.516	0.683 0.591 0.513 0.490 0.533 0.611 0.539	0.528 0.38 0.317 0.508 0.355 0.415 0.505	Qat 0.529 0.559 0.514 0.595 0.238 0.588 0.432	Qc 0.955 0.891 0.875 0.242 0.556 0.413 0.587	0.913 0.761 0.814 0.220 0.792 0.461 0.577	0.695 0.619 0.776 0.316 0.652 0.597 0.630	0.727 0.649 0.647 0.412 0.513 0.51 0.541